Springer
Acta Mechanica Sinica

• RESEARCH PAPER •

Acta Mech. Sin., Vol. 41, 324127 (2025)
https://doi.org/10.1007/s10409-024-24127-x

Verification and validation of a numerical wave tank with momentum source wave generation

Housheng Zhang[1], Yijing Hu[2], Biao Huang[2], and Xin Zhao[1*]

[1] *School of Aerospace Engineering, Beijing Institute of Technology, Beijing 100081, China;*
[2] *School of Mechanical Engineering, Beijing Institute of Technology, Beijing 100081, China*

Received May 23, 2024; accepted May 27, 2024; published online August 22, 2024

A systematic verification and validation (V&V) of our previously proposed momentum source wave generation method is performed. Some settings of previous numerical wave tanks (NWTs) of regular and irregular waves have been optimized. The H2-5 V&V method involving five mesh sizes with mesh refinement ratio being 1.225 is used to verify the NWT of regular waves, in which the wave height and mass conservation are mainly considered based on a Lv3 ($H_s = 0.75$ m) and a Lv6 ($H_s = 5$ m) regular wave. Additionally, eight different sea states are chosen to validate the wave height, mass conservation and wave frequency of regular waves. Regarding the NWT of irregular waves, five different sea states with significant wave heights ranging from 0.09 m to 12.5 m are selected to validate the statistical characteristics of irregular waves, including the profile of the wave spectrum, peak frequency and significant wave height. Results show that the verification errors for Lv3 and Lv6 regular wave on the most refined grid are −0.018 and −0.35 for wave height, respectively, and −0.14 and for −0.17 mass conservation, respectively. The uncertainty estimation analysis shows that the numerical error could be partially balanced out by the modelling error to achieve a smaller validation error by adjusting the mesh size elaborately. And the validation errors of the wave height, mass conservation and dominant frequency of regular waves under different sea states are no more than 7%, 8% and 2%, respectively. For a Lv3 ($H_s = 0.75$ m) and a Lv6 ($H_s = 5$ m) regular wave, simulations are validated on the wave height in wave development section for safety factors $FS \approx 1$ and $FS \approx 0.5$-1, respectively. Regarding irregular waves, the validation errors of the significant wave height and peak frequency are both lower than 2%.

Verification and validation, Wave generation, Momentum source function, Regular wave, Irregular wave, Uncertainty estimation

Citation: H. Zhang, Y. Hu, B. Huang, and X. Zhao, Verification and validation of a numerical wave tank with momentum source wave generation, Acta Mech. Sin. 41, 324127 (2025), https://doi.org/10.1007/s10409-024-24127-x

1. Introduction

Viscous numerical wave tanks (NWTs) have been widely employed to study water wave dynamics and the interaction of water waves with structures with the advancement of computational performance. For viscous NWTs, the wave generation method mainly includes the physical wave generation method (such as moving-boundary wave generation method [1,2]), static-boundary wave generation method [3,4], setting generation region where the velocity or other physical quantity are designated, viscous-potential flow decomposition method [5,6], and the source function method [7-10]. Compared with other wave generation methods, the source function method is advantageous in terms of numerical stability, applicability, implementability and computational efficiency. The source function method could be further divided into the mass source function method and the momentum source function method. By constructing different mass source functions, Lin and Liu [7] realized the generation of linear regular wave, irregular wave, Stokes wave, solitary wave and elliptical cosine waves. Based on Boussinesq models, Wei et al. [11] derived a mass source function and a momentum source function that can accurately simulate regular and random waves.

---

*Corresponding author. E-mail address: 6120160101@bit.edu.cn (Xin Zhao)
Executive Editor: Shizhao Wang

Furthermore, Choi and Yoon [8] and Ha et al. [9] applied Wei's momentum source function to three-dimensional viscous NWT, and the expected regular and irregular waves are produced. For fifth-order Stokes wave, Wang and Gao [10] combined velocity-inlet boundary with momentum source function to ensure the accuracy of wave propagation, and the effectiveness of wave generation with different steepness is verified.

However, due to limitations such as the deficiency of physical models and insufficient computing power, numerical simulations cannot completely reproduce reality. It is crucial to evaluate the error and uncertainty to represent the credibility of numerical simulation. Although much effort has been devoted to NWTs, almost all researchers have focused on mesh independence tests and the comparison of simulations with experiments. The estimation of modelling and numerical error using verification and validation for NWTs is also necessary and has gained more attention recently [12-17].

Verification and validation are two main principles that can be used to evaluate the reliability of computational fluid dynamics (CFD). The AIAA Committee [18] on Standards for Computational Fluid Dynamics published the Guide for the Verification and Validation of Computational Fluid Dynamics Simulations. Generally, verification refers to the process of determining the degree to which a computational simulation represents the conceptual model, and validation refers to the process of determining if a computational simulation represents real-world scenarios. Reynolds-averaged Navier-Stokes (RANS) simulations are usually used for viscous NWTs, and various V&V methods have been developed to obtain quantitative uncertainty estimations, including the grid convergence index [19], correction factor [20] method and factor of safety [21]. Wang et al. [15] and Wang and Chen [17] conducted V&V on the hydrodynamic responses of a mooring system under regular waves and irregular waves. Moreover, in their study, the numerical errors were quantified as statistical, iterative and discretization uncertainties. The results showed that the discretization uncertainty accounts for most of the verification uncertainty, and the validation of most concerned metrics could be achieved within the validation uncertainty by utilizing the dynamic mooring system. Using four uncertainty analysis methods, Islam and Guedes Soares [12] performed a systematic verification study of the wave loads on a fixed vertical cylinder based on a RANS-based NWT and compared a constant Courant-Friedrichs-Lewy (CFL) number-based uncertainty estimation method (UEM) to grid and time-independent procedures. The results showed that the CFL number-based method could provide more stable uncertainty results and may be more suitable for uncertainty estimation in CFD. Recently, Yu et al. [13] proposed a novel 2D NWT based on implicit filtered large eddy simulations (LESs) and demonstrated the accuracy and convergence rate with a focus on wave generation and propagation. However, the numerical errors were quantified by only the difference between the numerical and theoretical solutions, which is not a technical numerical error but a validation error, which refers to the difference of simulation with truth in this paper. In contrast to RANS simulations, LESs are based on multiscale models, and their V&V should be performed simultaneously [22]. Vreman et al. [23] firstly decomposed the verification error of an LES into two sources resulting from the discretization and the subgrid-scale (SGS) model, respectively, i.e., the numerical error and modelling error. Xing [24] further derived a general framework for LES V&V, by which the quantitative estimations of the numerical error, the modelling error, their coupling, and the associated uncertainties could be achieved.

With the rapid increase of using NWTs for wave research and wave-structure interaction, it is imperative to quantitatively estimate the numerical and modelling errors and associated uncertainties, which will provide guidelines for estimating the risk and reliability of the NWT-based designs, and help to optimize a wave simulation to obtain a minimum total simulation error. Previously, we proposed a NWT based on the momentum source function and applied it to investigate wave-cylinder interaction [25]. The objective of this paper is to conduct comprehensive and systematic verification and validation on the NWT. The H2-5 V&V method [24] is adopted to evaluate the modelling and numerical error under two sea states, and the metrics mainly include the wave height and mass conservation during long simulation. Regular waves under eight different sea states and irregular waves under five different sea states are validated, with focuses on the wave height, mass conservation, wave frequency and wave spectrum.

2. Method

2.1 Mathematical model

The incompressible viscous Navier-Stokes equation is adopted to solve the wave field:

$$\nabla \cdot \mathbf{U} = 0, \tag{1}$$

$$\frac{\partial \mathbf{U}}{\partial t} + (\mathbf{U} \cdot \nabla)\mathbf{U} = -\frac{1}{\rho} \nabla p + \frac{\mu}{\rho} \nabla \cdot (\nabla \mathbf{U}) + \mathbf{g} + \mathbf{f}_\sigma + \mathbf{f}_w + \mathbf{f}_d, \tag{2}$$

where $\mathbf{U} = [u, v, w]$ is the velocity vector; p is pressure; $\mathbf{g}$ is gravitational acceleration; $\mathbf{f}_\sigma$ is the surface tensor; $\mathbf{f}_w$ and $\mathbf{f}_d$ are the momentum source functions for wave generation and absorption, respectively; and ρ and μ are the mixing density and dynamic viscosity, respectively:

$$\rho = \alpha_l \rho_w + (1 - \alpha_l)\rho_a, \tag{3}$$

$$\mu = \alpha_l \mu_w + (1-\alpha_l)\mu_a, \tag{4}$$

where ρ_w and ρ_a are the densities of water and air, respectively, and α_l is the volume fraction of water.

The volume-of-fluid (VOF) method [26] is applied to solve gas-liquid flow, and the governing equation of the volume fraction transport is represented as follows:

$$\frac{\partial \alpha_l}{\partial t} + \mathbf{U}\cdot\nabla\alpha_l = 0. \tag{5}$$

2.2 Momentum source function

The momentum source function for regular wave generation is expressed as follows [25]:

$$f_{wx} = \frac{\partial u_w}{\partial t} = Akg\frac{\cosh k(h+z)}{\cosh kh}\sin(kx-\omega t), \tag{6}$$

$$f_{wz} = \frac{\partial w_w}{\partial t} = -Akg\frac{\sinh k(h+z)}{\cosh kh}\cos(kx-\omega t), \tag{7}$$

where h is the water depth, k denotes wave number, A is the wave amplitude, g is the gravitational acceleration, ω is the angular frequency, t represents time, x is the direction along which wave propagate, z is the vertical coordinate of NWT, and $z = 0$ represents the static water surface. The dispersion relationship is given by the following expression:

$$\omega^2 = kg\tanh(kh). \tag{8}$$

For irregular waves, the momentum source function can be calculated by the superposition of regular wave generation as follows:

$$f_{wx} = \sigma\sum_{n=1}^{N} a_n k_n g\frac{\cosh k(z+h)}{\cosh kh}\sin(k_n x - \omega_n t + \varepsilon_n), \tag{9}$$

$$f_{wz} = -\sigma\sum_{n=1}^{N} a_n k_n g\frac{\sinh k(z+h)}{\cosh kh}\cos(k_n x - \omega_n t + \varepsilon_n), \tag{10}$$

where σ is an energy scale factor that is used to prevent the excessive growth of wave amplitudes, which should match the width of the wave generation zone. Moreover, N is the total number of constituent waves, a_n is the amplitude of the nth constituent wave, k_n and ω_n are the wavenumber and circular frequency of the nth constituent wave, respectively, t is time, and ε_n is the random phase of the nth constituent wave and is distributed uniformly and randomly in the range of $[0, 2\pi)$.

2.3 Wave absorbing method

At the end, the wave dissipation section is applied opposite to the wave generation section of the NWT to damp the incoming wave. The momentum source function for wave dissipation is expressed by the following equation:

$$\mathbf{f}_d = -C(x)\mathbf{U}, \tag{11}$$

where $C(x)$ is the damping coefficient [27] that can be expressed as follows:

$$C(x) = \alpha\frac{\exp\left[\left(\dfrac{x-x_{\text{in}}}{x_{\text{out}}-x_{\text{in}}}\right)^n\right]-1}{\exp(1)-1}, \quad x_{\text{in}} < x < x_{\text{out}}, \tag{12}$$

where x_{in} and x_{out} are the inlet and outlet positions of the wave dissipation section along the wave propagating direction, respectively. α and n are the empirical parameters and are taken as $n = 10$ and $\alpha = 200$ [28]. The damping coefficient is only defined in the wave absorber zone and is always zero outside the absorber zone.

2.4 Numerical solution method

The projection method [29] is used for numerical solution. The liquid volume fraction of the next timestep is solved by the advection equation. The pressure term, diffusion term, gravity acceleration, surface tension and momentum source function for wave generation and dissipation are first ignored in the N-S equation, and the estimated velocity $\mathbf{U}^*$ of the next time step is solved by only considering the convection term:

$$\frac{\partial \alpha_l^{n+1}}{\partial t} = -\mathbf{U}^n\cdot\nabla\alpha_l^n, \tag{13}$$

$$\frac{\partial(\rho\mathbf{U}^*)}{\partial t} = -\nabla\cdot(\rho\mathbf{U}^n\mathbf{U}^n), \tag{14}$$

where the time derivative is discretized by the first-order forward difference, and the convection term is discretized by the second-order upwind scheme. Before solving the advection equation, the gas-liquid interface is approximated by the piecewise linear interface calculation (PLIC) method [26].

Second, the diffusion term is used to update the estimated velocity from $\mathbf{U}^*$ to $\mathbf{U}^{**}$:

$$\frac{\partial(\rho\mathbf{U}^{**})}{\partial t} = \nabla\cdot(\mu\nabla\mathbf{U}^*). \tag{15}$$

In this step, the alternating direction implicit difference method (ADI) is used for discretization.

Third, the pressure field p^{n+1} is solved based on the pressure Poisson equation:

$$\nabla\cdot\left(\frac{1}{\rho^n}\nabla p^{n+1}\right) = \frac{\nabla\cdot\mathbf{U}^{**}}{\Delta t}. \tag{16}$$

The successive overrelaxation (SOR) iterative method is adopted to solve the Poisson equation:

$$p_i^{n+1} = \lambda\left[\frac{1}{\rho}\left(\frac{p_{i-1}^n+p_{i+1}^n}{\Delta x^2}+\frac{p_{j-1}^n+p_{j+1}^n}{\Delta y^2}+\frac{p_{k-1}^n+p_{k+1}^n}{\Delta z^2}\right) + \frac{\nabla\cdot\mathbf{u}^{**}}{\Delta t}\right] \Bigg/ \frac{1}{\rho}\left(\frac{1}{\Delta x^2}+\frac{1}{\Delta y^2}+\frac{1}{\Delta z^2}\right) + (1-\lambda)p_i^n. \tag{17}$$

Finally, the velocity field of the next time step is updated by using the pressure term and body force:

$$\frac{\mathbf{U}^{n+1}-\mathbf{U}^{**}}{\Delta t} = -\frac{1}{\rho^{n}}\nabla p^{n+1} + \mathbf{g} + \mathbf{f}_{\sigma} + \mathbf{f}_{w} + \mathbf{f}_{d}, \tag{18}$$

where the surface tensor $\mathbf{f}_\sigma$ is modelled based on the continuum surface force (CSF) [30] model and height function method [31,32].

2.5 Uncertainty estimation methods

The direct viscous-flow simulation [33] is adopted for the present numerical solution, whose accuracy can be assessed through the UEM, primarily involving verification and validation. The verification error δ_v consists of the modelling error δ_M and the numerical error δ_N. The modelling error δ_M results from the difference between the mathematical model y_model and the physical reality y_nature:

$$\delta_M = y_\mathrm{model} - y_\mathrm{nature}. \tag{19}$$

The numerical error δ_N consists of δ_{N1} and δ_{N2}. The error δ_{N1} results from the difference between the analytical solution y_model of the mathematical model and the perfect solution $y_\mathrm{Pcomputer}$ of the discrete equations with the discretization size approaching zero.

$$\delta_{N1} = y_\mathrm{Pcomputer} - y_\mathrm{model}. \tag{20}$$

The error δ_{N2} comes from the difference between the perfect solution $y_\mathrm{Pcomputer}$ and the practical discrete solution y_sim, which is influenced by both spatial and temporal discretization, iterative convergence criterion and computer round off errors.

$$\delta_{N2} = y_\mathrm{sim} - y_\mathrm{Pcomputer}. \tag{21}$$

The validation error is represented by the comparison error E between the experimental measurement y_exp and the numerical solution y_sim.

$$E = y_\mathrm{exp} - y_\mathrm{sim} = \delta_\mathrm{exp} - \left(\delta_N + \delta_M\right), \tag{22}$$

where $\delta_\mathrm{exp} = y_\mathrm{exp} - y_\mathrm{nature}$. The above verification and validation concept is depicted in detail in Fig. 1.

To investigate the error characteristics of the present NWT using direct viscous-flow simulation, the numerical error δ_N and the modelling error δ_M could be evaluated based on the H2-5 V&V method [24,33]:

$$\delta_N + \delta_M = c_N (h^*)^{P_N} + c_M \varDelta^{P_M}, \tag{23}$$

where c_N and c_M are the underdetermined coefficients, and p_N and p_M are the orders of the accuracy of the numerical and modelling errors, respectively. $\varDelta$ is the local grid spacing h. The local spatial and temporal resolution h^* is defined as follows:

$$h^* = \sqrt{h\Delta t}, \tag{24}$$

where Δt is the timestep and h is the local grid spacing, which is obtained by $h = V^{1/3}$, where V is the volume of the computational cell.

The five-equation method, including five equations based on five sets of systematic refined grids, h, rh, r^2h, r^3h, and r^4h, is used to estimate the numerical and modelling errors.

$$\begin{aligned}
y_\mathrm{sim1} - y_\mathrm{model} &= c_N (h^*)^{P_N} + c_M \varDelta^{P_M},\\
y_\mathrm{sim2} - y_\mathrm{model} &= c_N (rh^*)^{P_N} + c_M (r\varDelta)^{P_M},\\
y_\mathrm{sim3} - y_\mathrm{model} &= c_N (r^2h^*)^{P_N} + c_M (r^2\varDelta)^{P_M},\\
y_\mathrm{sim4} - y_\mathrm{model} &= c_N (r^3h^*)^{P_N} + c_M (r^3\varDelta)^{P_M},\\
y_\mathrm{sim5} - y_\mathrm{model} &= c_N (r^4h^*)^{P_N} + c_M (r^4\varDelta)^{P_M},
\end{aligned} \tag{25}$$

where r is the mesh refinement ratio between the adjacent two sets of grids.

Furthermore, the numerical simulation could be validated through $|E| < U_V$. U_V is the validation uncertainty that can be obtained as follows:

$$U_V^2 = U_D^2 + U_\mathrm{sim}^2, \tag{26}$$

where U_D is the experimental uncertainty, which is zero for the current study. Generally, the simulation uncertainty U_sim is obtained by adopting a safety factor FS as follows:

$$U_\mathrm{sim} = FS\left|\delta_M + \delta_N\right|. \tag{27}$$

3. Results and discussion

3.1 Verification and validation of regular wave generations

According to the Chinese national standard GB/T 42176-2022 set by the Ministry of Natural Resources, ten grades

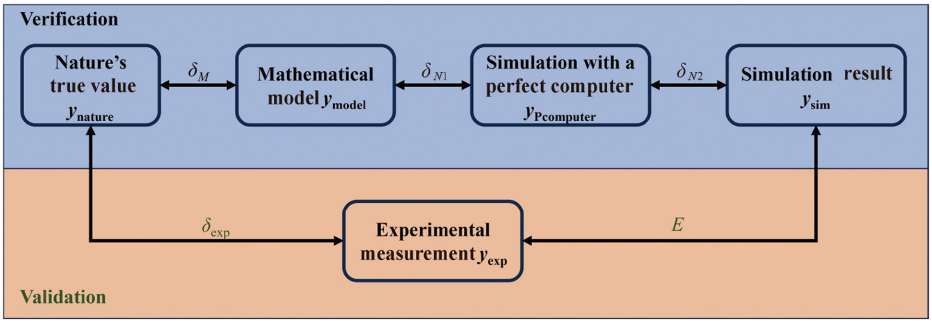

Figure 1 Error sources, verification and validation.

are divided to represent the intensity of the sea wave. The height of the significant wave H_s or the height of the highest one-tenth wave $H_{1/10}$ is the main principle to conduct the division, which is similar to Douglas Sea Scales. As shown in Table 1, eight sea states are selected to conduct the verification and validation for regular waves, corresponding to eight grades of wave heights, and all have the same wave steepness $\delta = H_s/\lambda = 1/30$.

Table 1 Wave parameters of regular waves for sea state Lv1-8

Sea state	Wave height H_s (m)	Wave period T (s)
Lv1	0.05	0.98
Lv2	0.3	2.41
Lv3	0.75	3.81
Lv4	2	6.21
Lv5	3.2	7.86
Lv6	5	9.83
Lv7	7.5	12.03
Lv8	11	14.57

The computational domain and boundary conditions of the NWT of a regular wave are shown in Fig. 2. Three sections, the wave generation section L_g, wave development section L_e and wave dissipation section L_d, are divided. The wall boundary condition is applied in the start position of the wave generation section and the end position of the wave dissipation section, and the free slip boundary condition is applied in the four side faces. The size of the computational domain is represented by the wavelength λ of the regular wave and occupies $8\lambda\times0.4\lambda\times\lambda$. The initial water depth is 0.5λ, and the lengths of the wave generation section, wave development section and wave dissipation section are 0.205λ, 4.795λ and 3λ, respectively.

The timestep Δt of the regular wave can be properly calculated by the following expression:

$$\Delta t = C_1\frac{\Delta x}{u_w}, \tag{28}$$

where C_1 is an empirical coefficient and $C_1 = 3/400$, which is determined by numerical tests. Δx is the mesh size along the x direction, and u_w is the wave velocity, which satisfies the following equation:

$$u_w = \frac{\lambda}{T} = \frac{\omega}{k}, \tag{29}$$

where T is the wave period, ω is the angular frequency, and $k = 2\pi/\lambda$ is the wavenumber.

A Lv3 regular wave (H_s = 0.75 m) is first selected to conduct the verification and validation. Figure 3 shows the verification and validation of the wave height and the mass conservation of the NWT under different mesh sizes with $\Delta x = \Delta z = 10\Delta y$. The results show that the validation error of mass conservation decreases as the grid is refined, while that of the wave height first decreases and then increases. The obvious convergence trend of the wave height and mass conservation could be observed from the last three mesh sizes, and the verification error δ_v (= $\delta_M + \delta_N$) of mass conservation is obtained based on H2-5 V&V method involving five mesh sizes, $\lambda/\Delta x = 26.6$, $\lambda/\Delta x = 32.6$, $\lambda/\Delta x = 40$, $\lambda/\Delta x = 48.9$ and $\lambda/\Delta x = 60$, which ensures that the mesh refinement ratio between the two adjacent mesh sizes remains constant and is 1.225. $m_{r,\mathrm{nature}}$ is the physical reality of mass conservation computed based on the H2-5 V&V method. The verification error of mass conservation on the most refined grid is $\delta_v = -0.14$, which is the sum of the modelling error $\delta_M = -1.96$ and the numerical error $\delta_N = 1.82$. This suggests that the modelling error suppresses the mass addition, while the numerical error promotes it. Therefore, mass conservation could be well achieved by the balance between the modelling error and the numerical error when the grid size is properly chosen. The verification estimation gives the convergence limit of mass conservation, which implies that complete mass conservation, that is, $m_r = 1$ and no validation error, could be realized with further mesh refinement. In addition, the verification error δ_v of the wave height is obtained based on the H2-5 V&V method involving three grid sizes, $\lambda/\Delta x = 40$, $\lambda/\Delta x = 48.9$ and $\lambda/\Delta x = 60$, where the orders of accuracy, p_N and p_M, are approximated by the results of mass conservation verification. $H_{\mathrm{num,nature}}$ is the physical reality of the wave height computed based on the H2-5 V&V method. The total error of the wave height is −0.018, but the limit of convergence seems to be larger than the analytical value $H_{\mathrm{num,nature}}$ in terms of the curve trend, which shows that the orders of accuracy of different physical

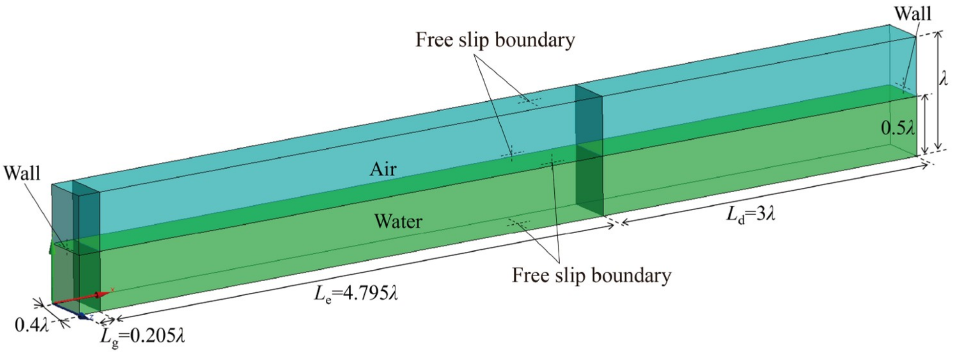

Figure 2 Fluid domain setup and boundary condition of NWT for regular waves.

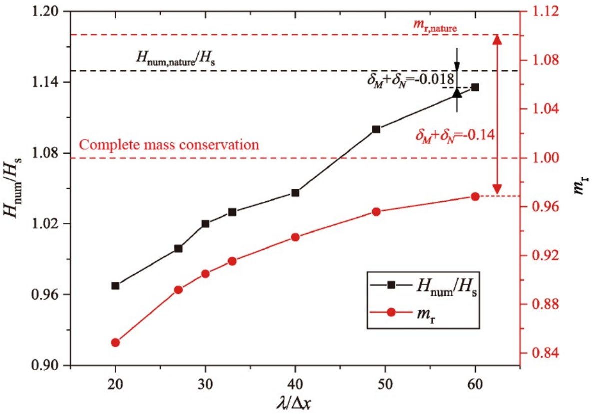

Figure 3 Verification of the wave height and mass conservation after eighteen wave periods for the Lv3 ($H_s = 0.75$ m) regular wave with $\Delta x = \Delta z = 10\Delta y$. The mass conservation is represented by the mass ratio $m_r = m_w/m_0$, where m_w is the mass of water after eighteen wave periods, and m_0 is the initial mass of water.

quantities may differ from each other. The three-dimensional wave surfaces with different mesh sizes are also shown in Fig. 4.

Additionally, the temporal evolution of the wave elevation at $x = 4\lambda$ and $z = 0.2\lambda$ and the spatial wave profile at the midplane $z = 0.2\lambda$ are plotted in Figs. 5 and 6, respectively. As shown in Fig. 6, for the low mesh density, the numerical error is relatively larger and results in an obvious decrease in the water surface. As the mesh is refined, the numerical error decreases, the mass conservation is well maintained, and the water surface descends less. The convergence trend of the water surface and mass conservation could be observed well from the results shown in Figs. 5 and 6. As the simulation time increases, the water surface will descend at an almost unchanged rate, which decreases as the mesh is refined, as shown in Fig. 5. Figure 6 shows that the NWT of the Lv3 regular wave remains almost isobathic along the wave propagation direction, although mass conservation is not always well achieved.

Figure 7 shows the results of the error estimation of the wave height on the most refined grid based on the H2-5 V&V method, where the experimental wave height used to calculate validation error is assumed to coincide with expected value with no experimental uncertainty. Strictly speaking, the error estimation method should satisfy some demands, including the evident convergence trend and the convergence rate between 0 and 1. Generally, the demands could be easily met for steady or statistical quantities to be measured, such as the water mass. However, for transient quantities, such as the local pressure, the H2-5 V&V method is hardly applied due to the poor convergence conditions. Even so, the transient wave height could be estimated by

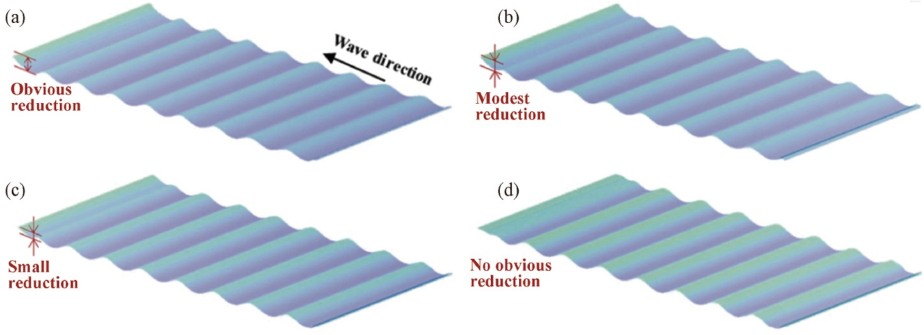

Figure 4 Three-dimensional wave surface of the Lv3 ($H_s = 0.75$ m) regular wave under different mesh sizes after eighteen wave periods. (a) $\lambda/\Delta x = 20$; (b) $\lambda/\Delta x = 40$; (c) $\lambda/\Delta x = 50$; (d) $\lambda/\Delta x = 60$.

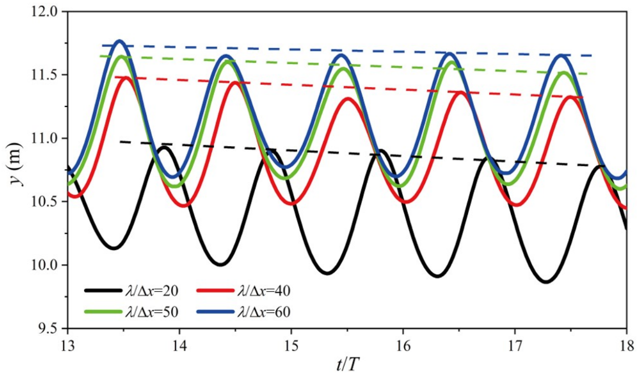

Figure 5 Convergence of the surface elevation of the Lv3 ($H_s = 0.75$ m) regular wave in the wave development section (the monitoring point is at $x = 4\lambda$, $z = 0.2\lambda$).

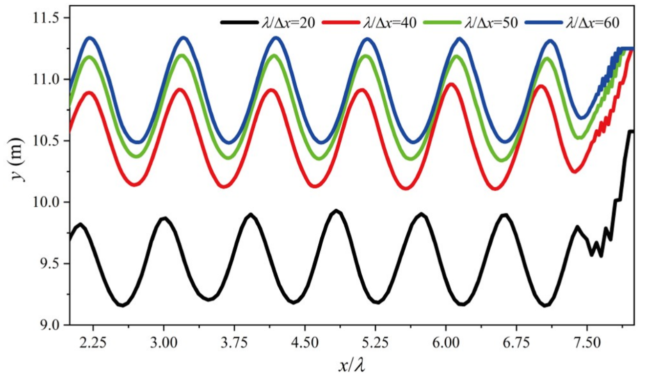

Figure 6 Convergence of the wave profile of the Lv3 ($H_s = 0.75$ m) regular wave in the wave development and dissipation sections at $z = 0.2\lambda$ after eighteen wave periods.

this method because it is relatively stable. Additionally, the error trend of the transient wave height along the wave propagation direction could be well recognized, although some errors are unreasonable. The results show that in the wave development section, total errors are approximately equal to validation errors, so the simulation could be easily validated based on safety factors $FS \approx 1$. Additionally, the model errors are relatively small and that the total error, that is, the verification error δ_v, mainly stems from the numerical error. In the wave development section, the total errors remain at approximately 14% and decrease slightly along the wave propagation direction. In the wave dissipation section, the total errors remain at approximately 10% and decrease slightly along the propagating direction, which show that the wave absorbing method could steadily dampen the incoming wave.

To briefly verify the convergence limit of mass conservation and considering the computational cost, the mesh size along the x- and z-directions is fixed at $\lambda/\Delta x = 40$ and $\Delta x = \Delta z$ and is simply refined along the y-direction. As shown in Fig. 8, the water mass throughout the fluid domain is larger than the initial mass m_0 after eighteen wave periods for $H_s/\Delta y = 32$, which shows that complete mass conservation could be achieved by selecting the proper mesh size. However, the wave height of the most refined mesh exceeds the previously predicted convergence limit, once again indicating that the orders of accuracy of different physical quantities on the same set of meshes are not always the same.

Then, a Lv6 regular wave ($H_s = 5$ m) is also selected to conduct the verification and validation. Figure 9 shows the verification and validation of the wave height and mass conservation. Mass conservation shows an obvious convergence trend as the grid size decreases. However, the wave height does not always increase as the mesh is refined and shows an oscillating and converging trend. Mass conservation is verified based on the H2-5 V&V method involving five mesh sizes, $\lambda/\Delta x = 26.6$, $\lambda/\Delta x = 32.6$, $\lambda/\Delta x = 40$, $\lambda/\Delta x = 48.9$ and $\lambda/\Delta x = 60$, with a mesh refinement ratio of 1.225. The verification error of mass conservation on the most refined grid is −0.17, including the modelling error $\delta_M < 1\times10^{-6}$ and numerical error $\delta_N = -0.17$, which shows that the numerical error is the main error and suppresses mass addition for the Lv6 regular wave at $\lambda/\Delta x = 60$. Complete mass conservation can be achieved by controlling the numerical error when the grid size further decreases. Additionally, the verification error of the wave height is obtained based on the H2-5 V&V method involving three grid sizes, $\lambda/\Delta x = 26.6$, $\lambda/\Delta x = 40$ and $\lambda/\Delta x = 60$, which allows the mesh refinement ratio to remain at 1.5. The total error of the wave height is −0.35, and the limit of convergence seems to approximate the analytical value $H_{num,nature}$ in terms of the curve trend. The three-dimensional wave surfaces of the Lv6 regular wave with different mesh sizes are also shown in Fig. 10. Meanwhile, the temporal evolution of the wave elevation and the spatial wave profile are shown in Figs. 11 and 12, respectively. As shown in Fig. 12, similar to the Lv3 regular wave, as the mesh is refined, the

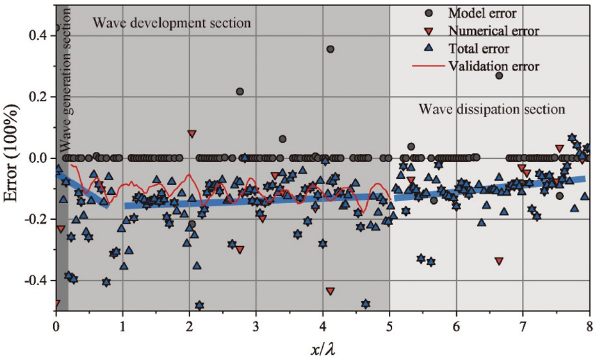

Figure 7 Error estimation of the wave height of the Lv3 ($H_s = 0.75$ m) regular wave throughout the fluid domain at $z = 0.2\lambda$ over the thirtieth wave period.

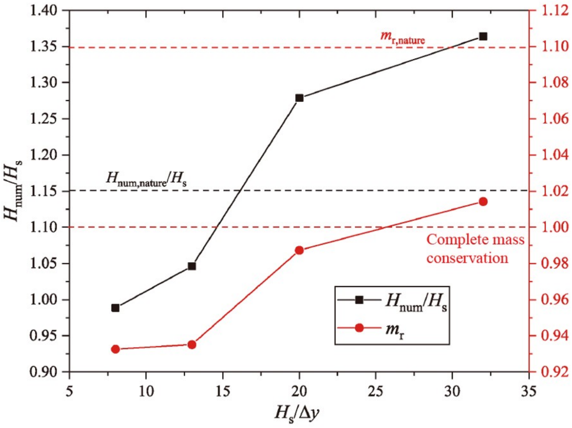

Figure 8 Verification of the wave height and mass conservation after eighteen wave periods for the Lv3 ($H_s = 0.75$ m) regular wave with $\lambda/\Delta x = 40$ and $\Delta x = \Delta z$.

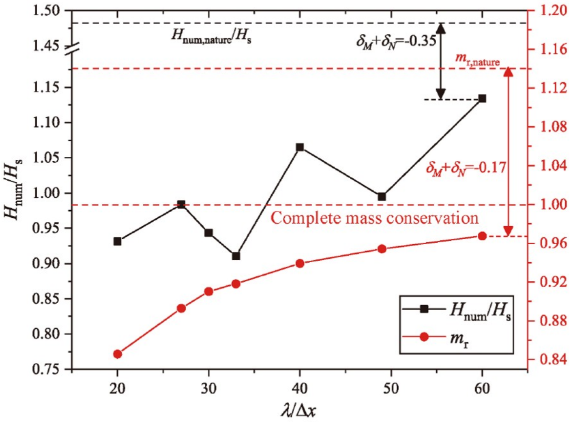

Figure 9 Verification of the wave height and mass conservation after eighteen wave periods for the Lv6 ($H_s = 5$ m) regular wave with $\Delta x = \Delta z = 10\Delta y$.

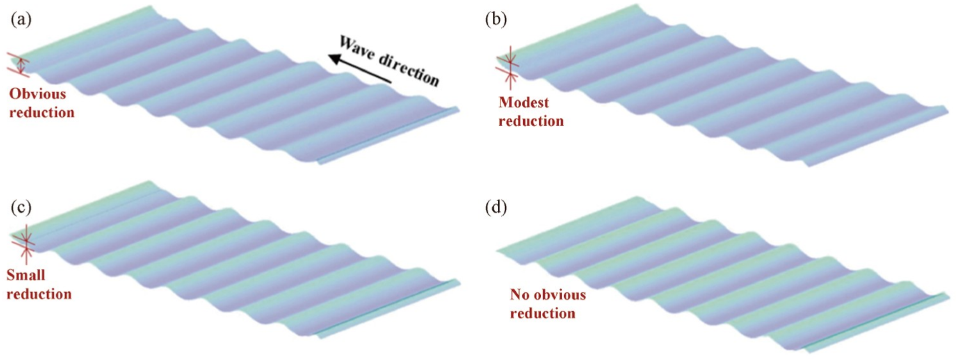

Figure 10 Three-dimensional wave surface of the Lv6 (H_s = 5 m) regular wave under different mesh sizes with $\Delta x = \Delta z = 10\Delta y$. (a) $\lambda/\Delta x$ = 20; (b) $\lambda/\Delta x$ = 26.6; (c) $\lambda/\Delta x$ = 40; (d) $\lambda/\Delta x$ = 60.

numerical error decreases, the mass conservation is well maintained, and the water surface descends less. As the simulation time increases, the water surface will descend at an almost unchanged rate, which decreases as the mesh is refined, as shown in Fig. 11. Figure 12 shows that the NWT of the Lv6 regular wave remains almost isobathic along the wave propagation direction. Furthermore, Fig. 13 shows the error estimation of the wave height over the thirtieth wave periods based on the H2-5 V&V method. The results show that in the wave development section, the validation errors are basically smaller than the total errors, and the simulation could be easily validated based on safety factors $FS \approx$ 0.5-1. Besides, the model errors are overall relatively small, and the total errors are dominated by the numerical errors. In the wave development section, the total errors remain at approximately −20% and increase slightly along the wave propagation direction. In the wave dissipation section, the total errors remain at approximately 10% and decrease slightly along the propagating direction, which indicates that the wave absorbing method could dampen the incoming wave effectively, and its errors are relatively small, which is also seen in Fig. 12.

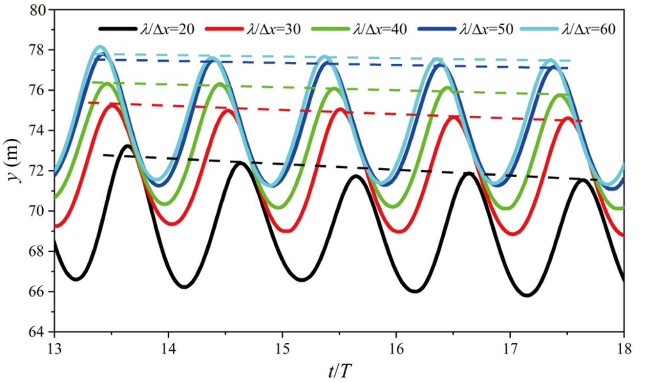

Figure 11 Convergence of the surface elevation of the Lv6 (H_s = 5 m) regular wave in the wave development section (the monitoring point is at x = 4λ, z = 0.2λ).

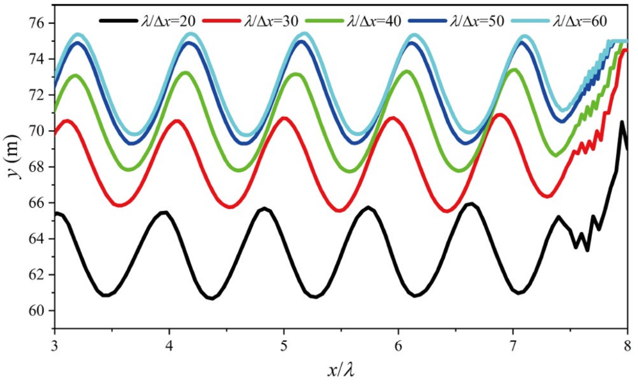

Figure 12 Convergence of the wave profile of the Lv6 (H_s = 5 m) regular wave in the wave development and dissipation sections at z = 0.2λ after eighteen wave periods.

To study the effect of the mesh size on the evolution of wave elevation, the horizontals of different wave evolutions are adjusted to coincide with each other, as shown in Fig. 14. Overall, the evolution curves under different grids are similar. The evolution periods do not have obvious differences. Figure 14(c) shows that the evolution amplitude increases slightly as the mesh is refined, which agrees with the results in Fig. 8. As shown in Fig. 14(b) and (c), the evolution shape approaches the analytical results better as the mesh is refined, although the evolution amplitude under

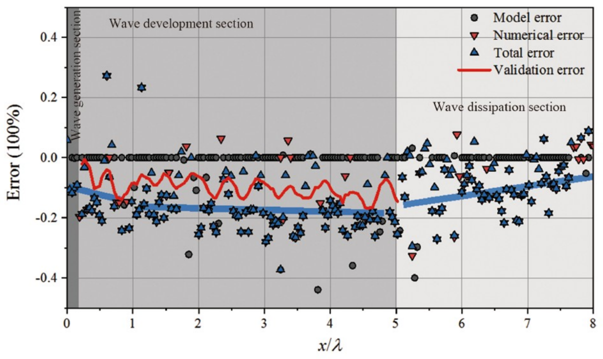

Figure 13 Error estimation of the wave height of the Lv6 (H_s = 5 m) regular wave throughout the fluid domain at midplane z = 0.2λ over the thirtieth wave periods.

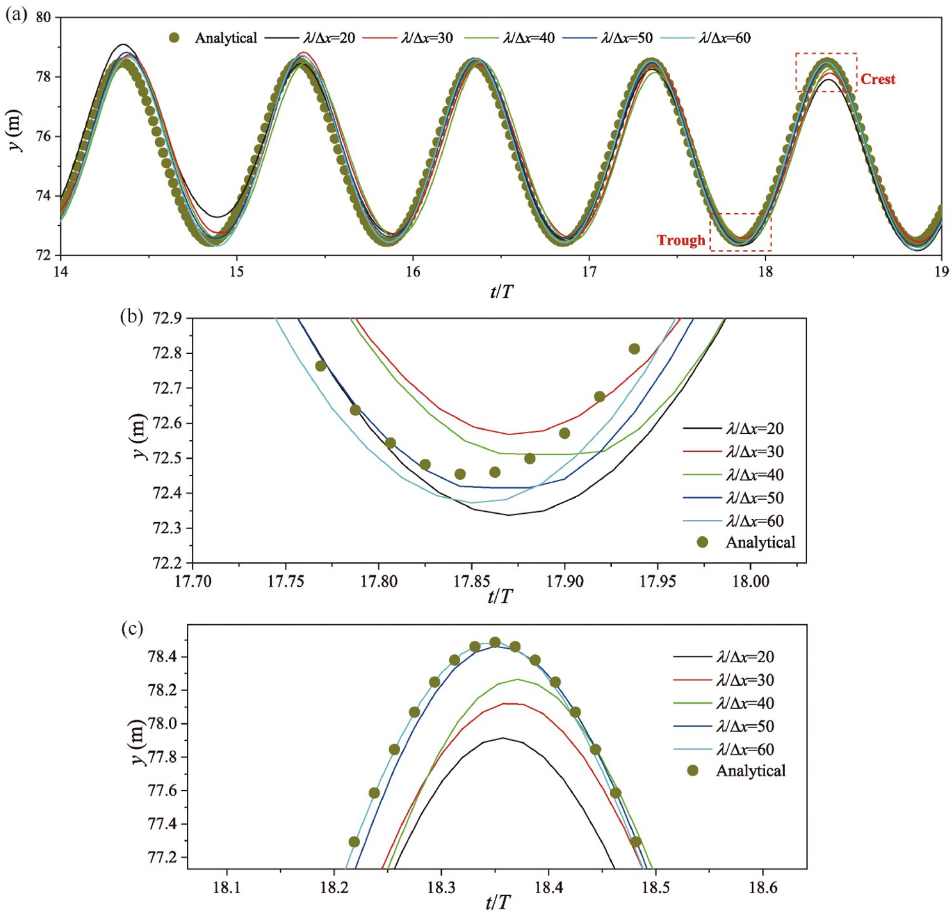

Figure 14 Evolution of the numerical surface elevation and the analytical shape of the Lv6 (H_s = 5 m) regular wave under different mesh sizes when the horizontals are adjusted to coincide with each other. The monitoring point is at point $x = 4\lambda$, $z = 0.2\lambda$. (a) Evolution of the wave elevation; (b) enlarged view of the crest; (c) enlarged view of the trough.

the most refined mesh is larger than the analytical solution, which results from the modelling error of the NWT. The elevation evolution curve under a mesh size of $\lambda/\Delta x$ = 60 coincides with the analytical curve on the crest region and is approximately parallelly coincident with the analytical solution on the trough region. The validation error of the wave elevation evolution is rather small when the mesh size is finer than $\lambda/\Delta x$ = 50. Additionally, a fast Fourier transform (FFT) is conducted for the wave elevation evolution under different mesh sizes, and the frequency spectrum is shown in Fig. 15. The results show that the peak frequency of the elevation evolution under different mesh sizes agrees well with the expected value ω = 0.0645 rad/s, which indicates that the frequency characteristics of regular waves could be well simulated by the present NWT.

Meanwhile, the influence of the grid size on the spatial profile distribution of regular waves is investigated, and Fig. 16 shows the wave profile distribution along the wave propagation direction with the horizontals of different waves adjusted to coincide with each other. In contrast to the temporal evolution of the wave elevation, disparities between various wave profiles are observed. As the mesh is refined, the amplitude of the wave profile increases obviously, and the wavelength gets closer to the expected value better, as shown in Fig. 16(a) and (c). However, the complete coincidence of the numerical profile with the analytical

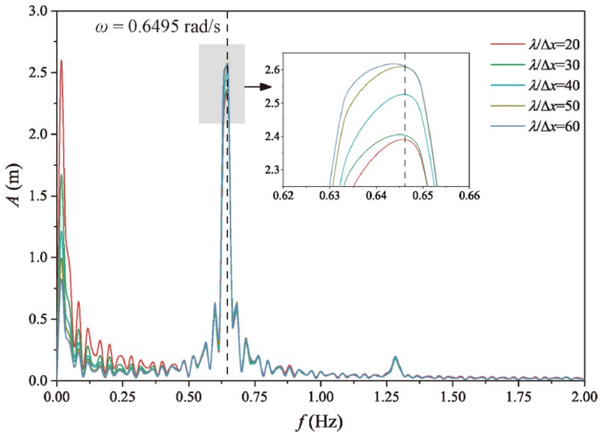

Figure 15 Frequency spectrum of the Lv6 (H_s = 5 m) regular wave under different mesh sizes.

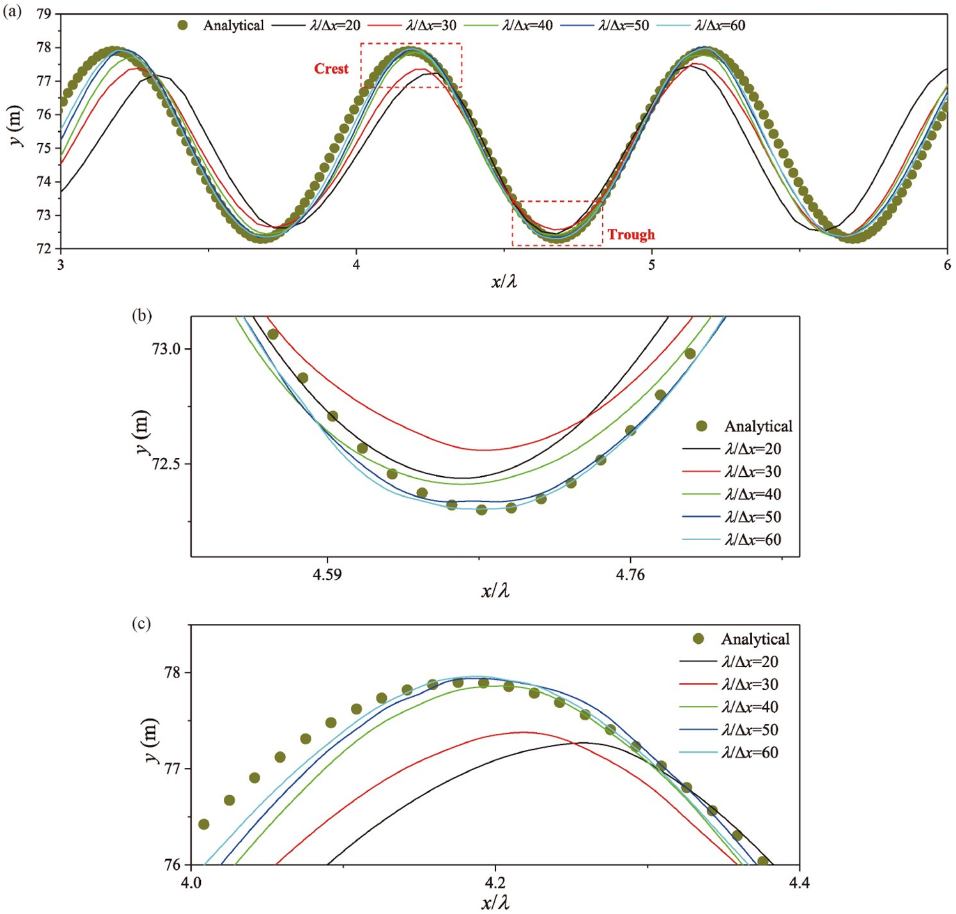

Figure 16 Numerical wave profile and the analytical profile of the Lv6 (H_s = 5 m) regular wave under different mesh sizes when the horizontals are adjusted to coincide with each other. The wave profile is located at the midplane $z = 0.2\lambda$ of the NWT. (a) Wave profile along the wave propagating direction; (b) enlarged view of the wave crest; (c) enlarged view of the wave trough.

profile does not occur as the mesh size decreases, which results from the modelling and numerical error of the present NWT and the resultant smaller wavelength. The wavenumber spectra under different mesh sizes are given in Fig. 17, and the theoretical wavenumber of the present Lv6 (H_s = 5 m) regular wave is marked. The results show that the peak wavenumber of the numerical waves appears around the analytical value, which indicates the good ability of the present NWT to simulate the wavenumber characteristics of regular waves.

Additionally, the other six grades of wave height shown in Table 1 are simulated, and the three-dimensional wave surface is shown in Fig. 18. The wave propagates from the right side to the left side, and the wave surfaces under different sea states look similar due to the same wave steepness and dimensional sizes. The numerical wave height and the remaining mass of water after ten wave periods are plotted in Fig. 19. The relative errors of the average wave height are all smaller than 7%, and the mass conservation remains good for all eight grades of wave height with at least 93.5% mass left after ten wave periods, representing the good ability of the present NWT to simulate the energy characteristics of regular waves ranging from Lv1 to Lv8 waves.

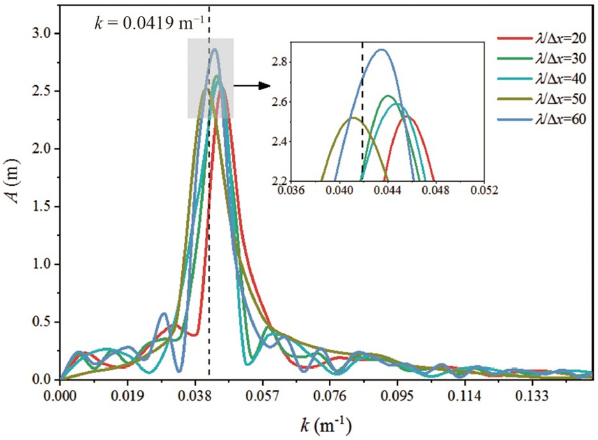

Figure 17 Wavenumber spectrum of the Lv6 (H_s = 5 m) regular wave under different mesh sizes.

The FFT is applied to the evolution of the water surface elevation under different sea states, and the results are shown in Fig. 20. The profiles of the frequency spectrum curve are similar, and only one dominant frequency exists in each regular wave. In addition, a small-amplitude peak frequency also occurs at approximately two times the dominant frequency, which results from the nonlinearity of the gravity water wave when the wave steepness is small. With the level of sea state increasing, the dominant frequency decreases. Figure 21 shows the dominant frequencies of the wave evolution under different sea states and

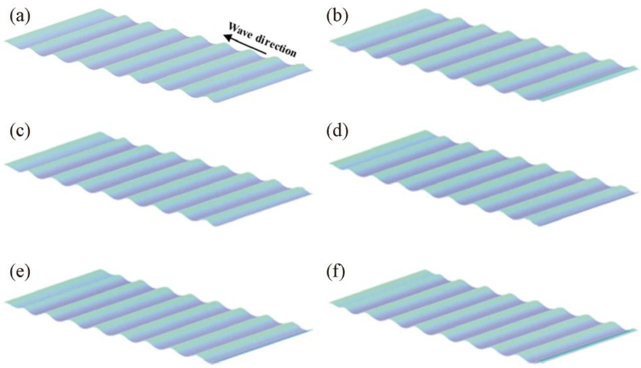

Figure 18 Three-dimensional wave surface under different sea states after ten wave periods, with $\lambda/\Delta x = 40$ and $\Delta x = \Delta z = 10\Delta y$. (a) Lv1, H_s = 0.05 m; (b) Lv2, H_s = 0.3 m; (c) Lv4, H_s = 2 m; (d) Lv5, H_s = 3.2 m; (e) Lv7, H_s = 7.5 m; (f) Lv8, H_s = 11 m.

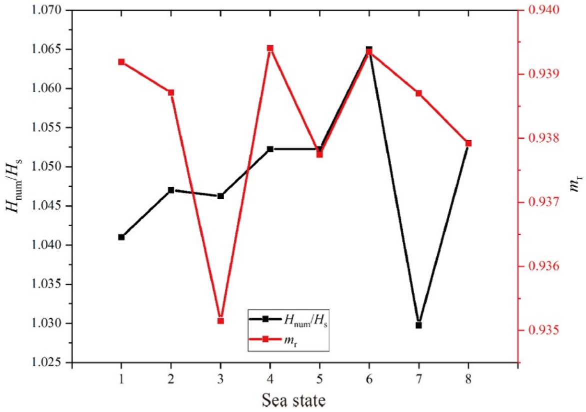

Figure 19 Numerical height H_{num} and the mass of water m_w after ten wave periods under different sea states. For simplicity, the mass of water is represented by the mass ratio $m_r = m_w/m_0$, where m_0 is the initial mass of water.

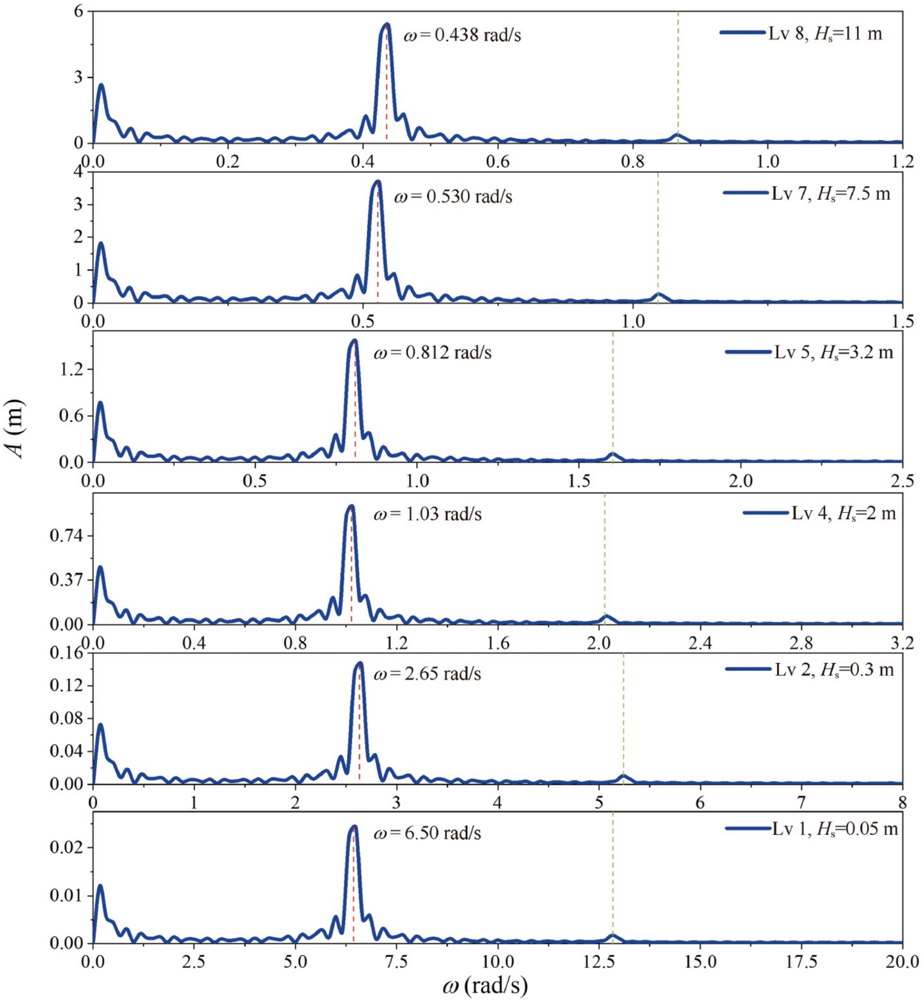

Figure 20 Frequency spectrum of the evolution of the water surface elevation under different sea states.

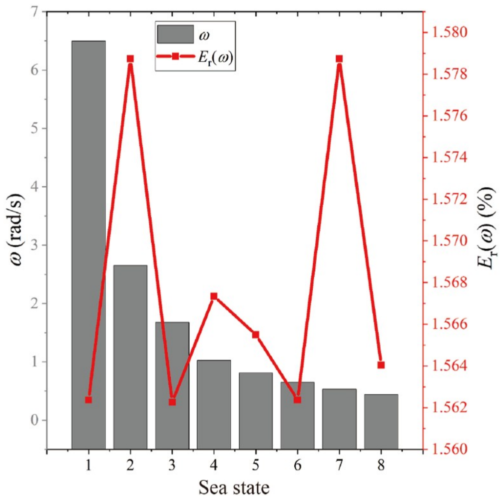

Figure 21 Dominant frequency of the wave elevation under different sea states.

the corresponding relative errors, which are compared with the input wave frequency and not larger than 2%, representing the good ability of the present NWT to simulate the frequency characteristics of regular waves ranging from Lv1 to Lv8 waves.

3.2 Validation of irregular wave generations

In addition to regular waves, irregular waves under different sea states are also simulated and validated. The computational domain and boundary conditions of the NWT of irregular waves are shown in Fig. 22. The configuration and boundary conditions of irregular NWTs are the same as those of regular NWTs. The size of the computational domain is represented by the wavelength λ_p corresponding to the peak frequency ω_p of the wave spectrum and occupies $3\lambda_p \times 0.02\lambda_p \times 0.4\lambda_p$. The initial water depth is $0.22\lambda_p$, and the lengths of the wave generation section, wave development section and wave dissipation section are the same, for which the energy scale factor in Eqs. (6) and (7) is set to $\sigma = 0.0969$. Considering the mesh density of the NWTs of regular waves, $\lambda_p/\Delta x = 200$ and $\Delta x = \Delta z = 3\Delta y$ are chosen for the NWTs of irregular waves. Moreover, the timestep is given by the following expression:

$$\Delta t = C_2 \frac{2\pi}{\omega_p}, \tag{30}$$

where C_2 is an empirical coefficient and set to 1/7500 according to numerical tests, which is sufficiently small for the current simulation.

Five grades of significant wave heights, including the Lv1, Lv3, Lv5, Lv6 and Lv8 sea states, are selected to conduct the simulations of irregular wavs, as shown in Fig. 23. The JONSWAP spectrum is chosen to be the input wave spectrum, and the formula is expressed as follows:

$$S(\omega) = \alpha g^2 \frac{1}{\omega^5} \exp\left[-\frac{5}{4}\left(\frac{\omega_p}{\omega}\right)^4\right] \gamma^{\exp\left[-(\omega-\omega_p)^2/\left(2\sigma^2\omega_p^2\right)\right]}, \tag{31}$$

where $\omega = 2\pi f$, f is the wave frequency in Hertz, $\alpha = 0.01816$ is the energy scale factor, g is the gravity acceleration, ω_p is the peak frequency, $\gamma = 3.3$ is the peak enhancement factor, σ is the spectral shape parameter, $\sigma = 0.07$ when $\omega \le \omega_p$ and $\sigma = 0.09$ when $\omega > \omega_p$. The peak frequency can be approximately obtained by the relation with the significant wave height as follows:

$$H_s = 4\sqrt{m_0}, \tag{32}$$

$$m_0 = \int S(\omega)\mathrm{d}\omega. \tag{33}$$

Then, the spectra for irregular waves under different sea states are shown in Fig. 24, and the section at $\omega \in [0.65\omega_p, 2\omega_p]$ of the original JONSWAP spectrum could be simply left due to its energy concentration characteristic. The random phase spectrum method (RPSM) [34,35] is used to calculate parameters in the momentum source.

Figure 25 shows the three-dimensional wave surface under different sea states, corresponding to the respective wave spectrum. The wave is generated in the wave generation section, develops under gravity in the wave development section and finally damps in the wave dissipation section. As shown in Fig. 25, the obvious wave is hardly observed at the end of the wave dissipation section. Therefore, the irregular wave could be damped well under the effect of the

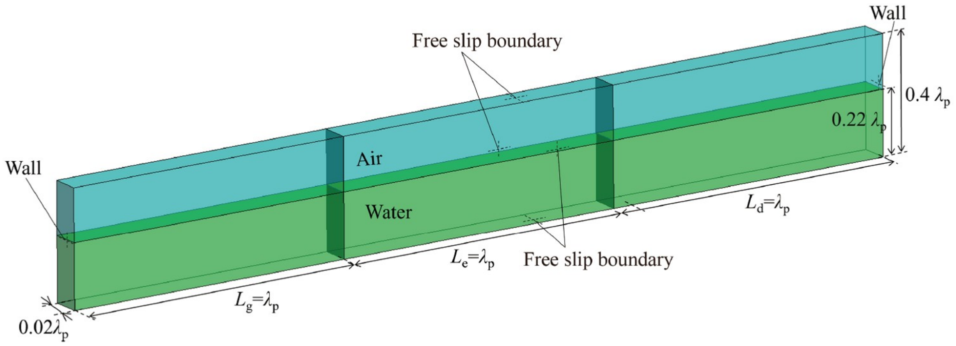

Figure 22 Fluid domain setup and boundary condition of the NWT for irregular waves.

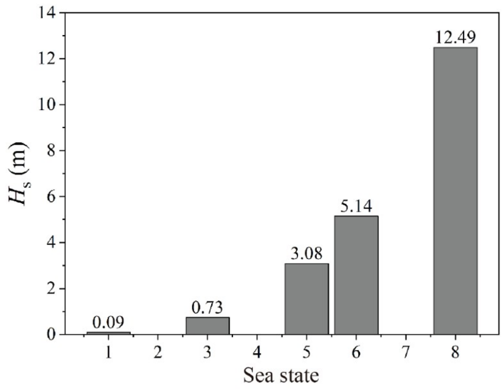

Figure 23 Height of the significant wave H_s irregular waves under different sea states.

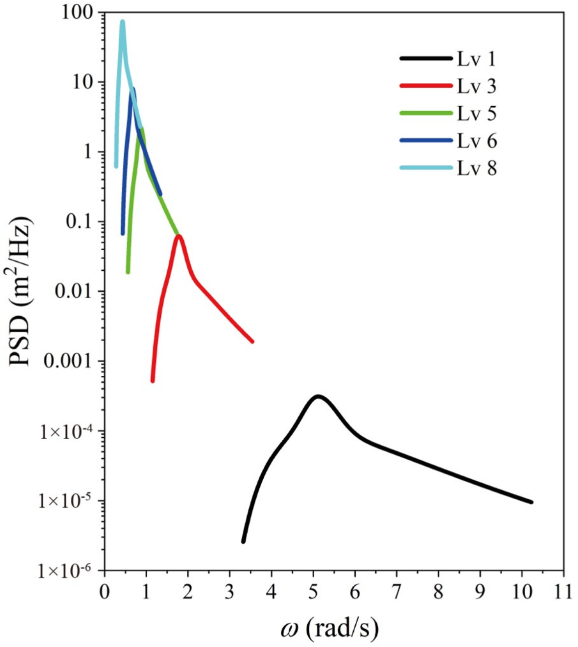

Figure 24 JONSWAP spectrum of the sea state involving Lv1-Lv8.

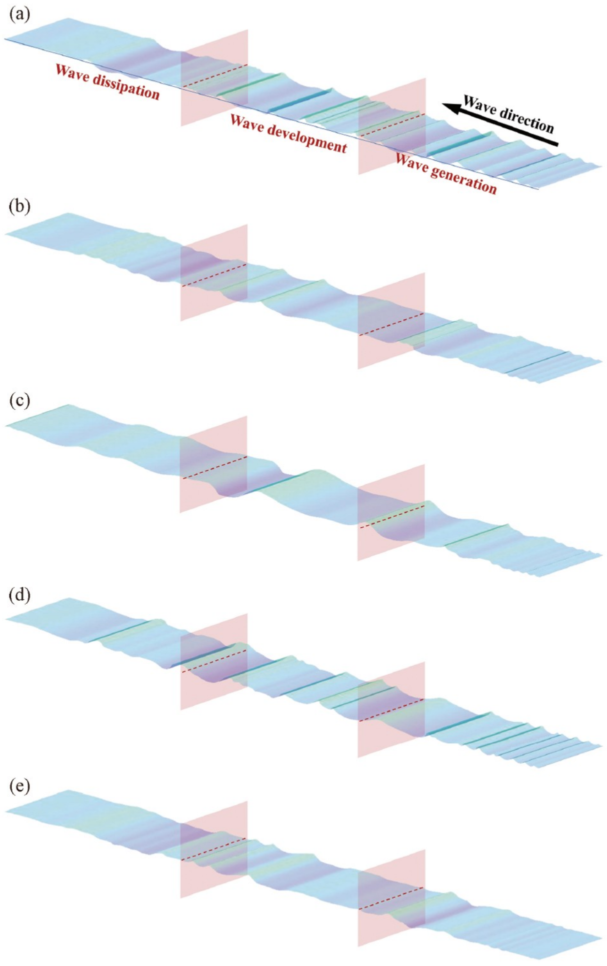

Figure 25 Three-dimensional wave surface of irregular waves under different sea states. (a) Lv1, $H_s = 0.088$ m; (b) Lv3, $H_s = 0.73$ m; (c) Lv5, $H_s = 3.08$ m; (d) Lv6, $H_s = 5.14$ m; (e) Lv8, $H_s = 12.49$ m.

wave-absorbing momentum source function. At the beginning of the wave generation section, small-amplitude and high-wavenumber waves emerge under the action of the wavemaker momentum source function. Then, those waves merge into relatively high-amplitude and low-wavenumber waves at the exit of the wave generation section. In the wave development section, waves develop without the effect of the momentum source function and finally evolve into external gravity waves. Figure 26 shows the power spectrum density function of the water surface elevation of different irregular waves and the corresponding input JONSWAP spectrum. The results show that the peak frequency and the curve profile of the numerical results agree well with the JONSWAP spectrum. Figures 27 and 28 show the significant wave height of irregular waves and the peak frequency under different sea states, of which the relative errors are both lower than 2%, representing the good ability of the present NWT to simulate the energy and frequency characteristics of irregular waves ranging from Lv1 to Lv8 waves.

4. Conclusion

The NWT of regular waves and irregular waves based on our previously proposed momentum source method [25] is systematically verified and validated, ranging from the Lv1 wave to the Lv8 wave. The NWT is composed of three sections: a wave generation section, a development section and a dissipation section. The H2-5 V&V method is used to evaluate the verification error, including the modelling error and numerical error. The verification and validation of the Lv3 (H_s = 0.75 m) and Lv6 (H_s = 5 m) regular waves are conducted based on five mesh sizes with mesh refinement ratio being 1.225 and timestep proportional to grid size. The verification errors for Lv3 and Lv6 regular wave on the most

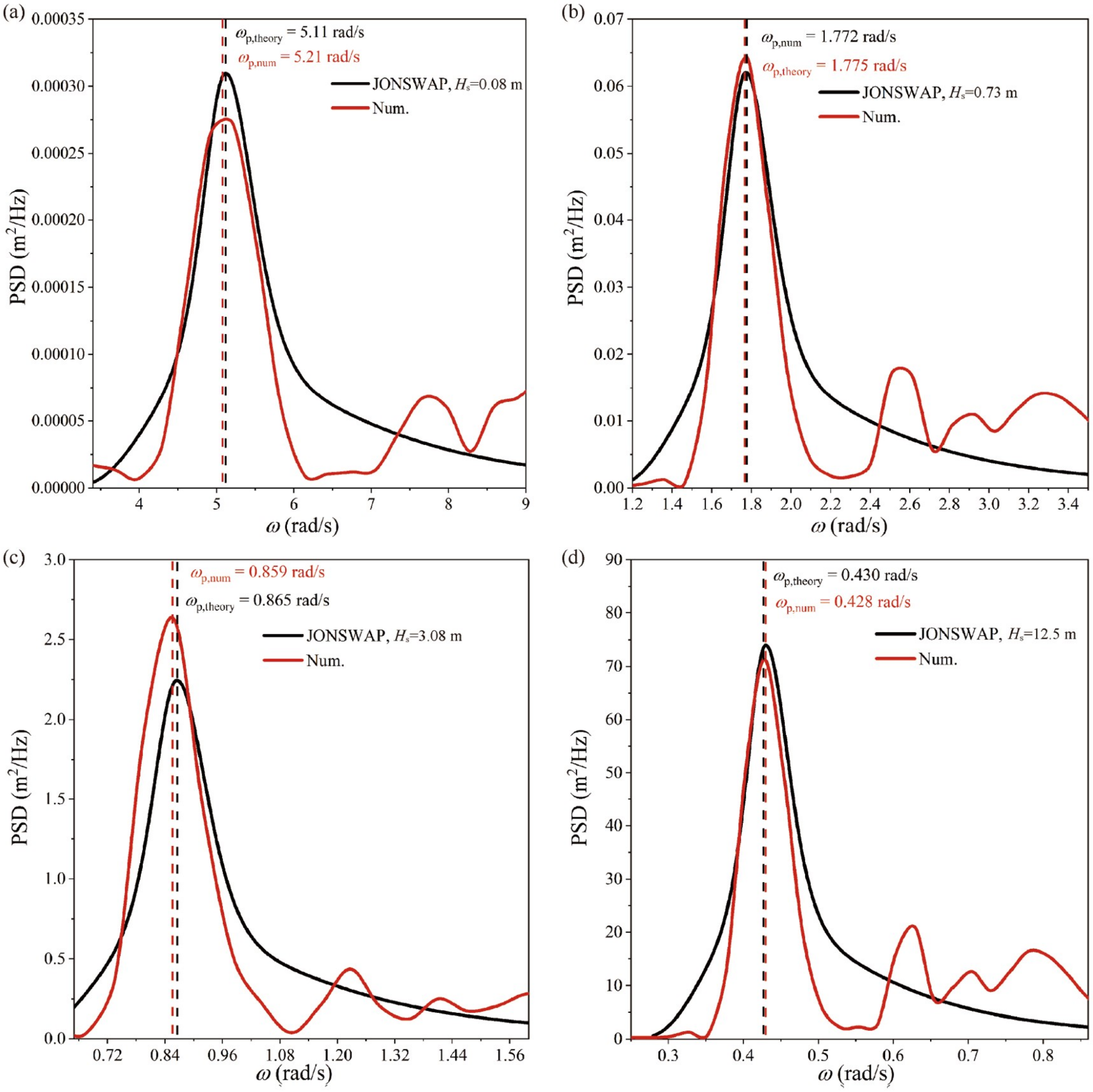

Figure 26 Power spectrum density of the wave surface elevation of irregular waves under different sea states. (a) Lv1; (b) Lv3; (c) Lv5; (d) Lv8.

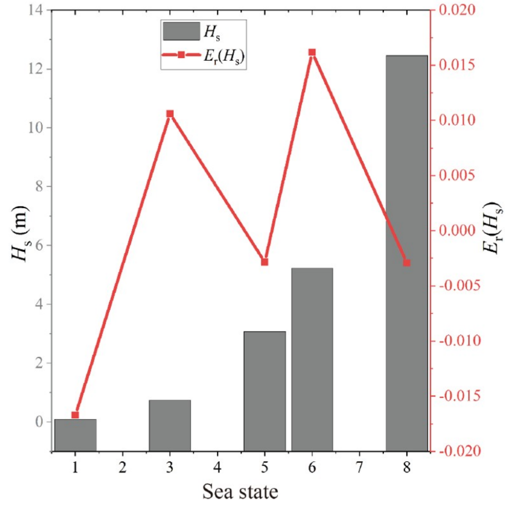

Figure 27 Significant wave height H_s of numerical results and its relative validation error $E_r(H_s)$ of irregular waves under different sea states.

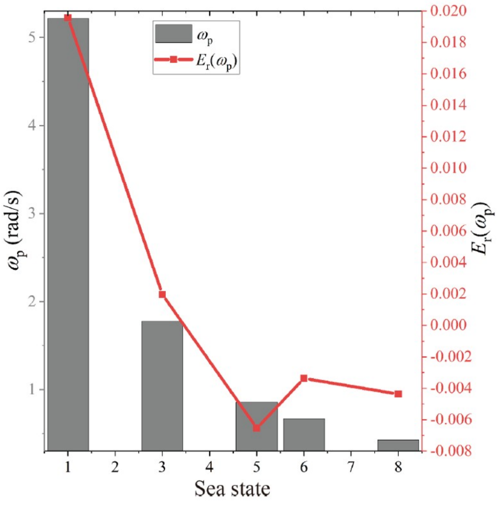

Figure 28 Peak frequency ω_p of numerical results and its relative validation error $E_r(\omega_p)$ of irregular waves under different sea states.

refined grid are −0.018 and −0.35 for wave height, respectively, and −0.14 and for −0.17 mass conservation, respectively. The modelling error and the numerical error could be balanced to realize the smaller validation error by adjusting the mesh size elaborately. Throughout the domain, the numerical error accounts for most of the total error. Overall, the wave height is slightly larger than the expected value, while the wavelength is slightly shorter than the analytical solution, which leads to a larger wave steepness. Simulations are validated on the wave height in wave development section for safety factors $FS \approx 1$ and $FS \approx 0.5$-1, for Lv3 and Lv6 regular waves, respectively. Regular waves ranging from Lv1 to Lv8 are validated with mesh sizes of $\lambda/\Delta x = 40$ and $\Delta x = \Delta z = 10\Delta y$. The relative errors of the wave height, mass conservation and dominant frequency under different sea states are smaller than 7%, 8% and 2%, respectively. The characteristics of regular waves, including the wave height, wavelength, frequency, evolution, and wave profile, could be realized well by the present NWT. Using the JONSWAP spectrum as the input spectrum, irregular waves under different sea states are also validated. The statistical characteristics are mainly compared with the theoretical values, and the results show that the spectrum profile of the wave elevation evolution agrees with the input JONSWAP spectrum. The significant wave height and peak frequency of the wave spectrum basically coincide with the theoretical value, and both errors are lower than 2%. Therefore, irregular waves under different sea states could also be simulated well by the present NWT.

Conflict of interest *On behalf of all authors, the corresponding author states that there is no conflict of interest.*

Author contributions *Housheng Zhang is responsible for formal analysis, investigation, methodology, visualization and writing, specifically including the numerical set-up and the results' processing, writing of the first draft of the manuscript, and presentation of the published work. Yijing Hu is responsible for formal analysis, methodology, validation and writing, specifically including application of mathematical techniques to analyze study data and design of V&V methodology. Biao Huang is responsible for supervision and writing, specifically including review & editing, oversight and the research activity planning and execution. Xin Zhao is responsible for conceptualization, supervision and writing, specifically including review & editing, formulation of overarching research goals, oversight and the research activity planning and execution.*

Acknowledgements *This work was supported by the National Key R&D Program of China (Grant No. 2022YFB3303500).*

1 A. Mahmoudi, H. Hakimzadeh, and M. J. Ketabdari, Simulation of wave propagation over coastal structures using WCSPH method, 2014.
2 P. Higuera, I. J. Losada, and J. L. Lara, Three-dimensional numerical wave generation with moving boundaries, Coast. Eng. **101**, 35 (2015).
3 Z. Z. Hu, D. Greaves, and A. Raby, Numerical wave tank study of extreme waves and wave-structure interaction using OpenFoam®, Ocean Eng. **126**, 329 (2016).
4 N. N. Peng, and K. W. Chow, A numerical wave tank with large eddy simulation for wave breaking, Ocean Eng. **266**, 112555 (2022).
5 T. Lao, Z. Li, Z. Wang, Z. Wang, and Z. Yang, Generation of incident wave in two-phase flow simulation based on field decomposition, Ocean Eng. **285**, 115256 (2023).
6 V. Vukčević, H. Jasak, and Š. Malenica, Decomposition model for naval hydrodynamic applications, Part I: Computational method, Ocean Eng. **121**, 37 (2016).
7 P. Lin, and P. L. F. Liu, Internal wave-maker for Navier-Stokes equations models, J. Waterway Port Coast. Ocean Eng. **125**, 207 (1999).
8 J. Choi, and S. B. Yoon, Numerical simulations using momentum source wave-maker applied to RANS equation model, Coast. Eng. **56**, 1043 (2009).
9 T. Ha, P. Lin, and Y. S. Cho, Generation of 3D regular and irregular waves using Navier-Stokes equations model with an internal wave maker, Coast. Eng. **76**, 55 (2013).
10 W. Wang, and Z. Gao, On the accuracy of large-steepness regular wave generation, propagation and run-up on a cylinder, Ocean Eng. **251**, 111088 (2022).
11 G. Wei, J. T. Kirby, and A. Sinha, Generation of waves in Boussinesq models using a source function method, Coast. Eng. **36**, 271 (1999).
12 H. Islam, and C. Guedes Soares, Assessment of uncertainty in the CFD simulation of the wave-induced loads on a vertical cylinder, Mar. Struct. **80**, 103088 (2021).
13 X. Yu, Y. Shao, D. R. Fuhrman, and Y. Zhang, A viscous numerical wave tank based on immersed-boundary generalized harmonic polynomial cell (IB-GHPC) method: Accuracy, validation and application, Coast. Eng. **180**, 104273 (2023).
14 Y. Wang, H. C. Chen, A. Koop, and G. Vaz, Verification and validation of CFD simulations for semi-submersible floating offshore wind turbine under pitch free-decay motion, Ocean Eng. **242**, 109993 (2021).
15 Y. Wang, H. C. Chen, A. Koop, and G. Vaz, Hydrodynamic response of a FOWT semi-submersible under regular waves using CFD: Verification and validation, Ocean Eng. **258**, 111742 (2022).
16 L. Wang, A. Robertson, J. Kim, H. Jang, Z. R. Shen, A. Koop, T. Bunnik, and K. Yu, Validation of CFD simulations of the moored DeepCwind offshore wind semisubmersible in irregular waves, Ocean Eng. **260**, 112028 (2022).
17 Y. Wang, and H. C. Chen, Verification and validation of computational fluid dynamic simulations of a FOWT semi-submersible under bichromatic and random waves, J. Offshore Mech. Arctic Eng. **145**, 062001 (2023).
18 AIAA, Guide: Guide for the Verification and Validation of Computational Fluid Dynamics Simulations (AIAA G-077-1998(2002)), (AIAA, Reston, 1998).
19 P. J. Roache, Verification and Validation in Computational Science and Engineering (Hermosa, Albuquerque, 1998).
20 F. Stern, R. V. Wilson, H. W. Coleman, and E. G. Paterson, Comprehensive approach to verification and validation of CFD simulations—Part 1: methodology and procedures, J. Fluids Eng. **123**, 793 (2001).
21 T. Xing, and F. Stern, Factors of safety for Richardson extrapolation, J. Fluids Eng. **132**, 061403 (2010).
22 Y. Long, X. Long, B. Ji, and T. Xing, Verification and validation of Large Eddy Simulation of attached cavitating flow around a Clark-Y hydrofoil, Int. J. Multiphase Flow **115**, 93 (2019).
23 B. Vreman, B. Geurts, and H. Kuerten, Comparision of numerical schemes in large-eddy simulation of the temporal mixing layer, Int. J. Numer. Meth. Fluids **22**, 297 (1996).
24 T. Xing, A general framework for verification and validation of large eddy simulations, J. Hydrodyn. **27**, 163 (2015).
25 H. Zhang, B. Huang, and X. Zhao, Numerical investigation of wave-cylinder interaction based on a momentum source wave generation method, Ocean Eng. **288**, 115893 (2023).
26 G. Tryggvason, A. Esmaeeli, J. Lu, and S. Biswas, Direct numerical simulations of gas/liquid multiphase flows, Fluid Dyn. Res. **38**, 660 (2006).
27 G. Wei, and J. T. Kirby, Time-dependent numerical code for extended

Boussinesq equations, J. Waterway Port Coast. Ocean Eng. **121**, 251 (1995).

28 P. Lin, and P. L. F. Liu, Discussion of "Vertical variation of the flow across the surf zone", Coast. Eng. **50**, 161 (2004).

29 A. J. Chorin, Numerical solution of the Navier-Stokes equations, Math. Comp. **22**, 745 (1968).

30 J. U. Brackbill, D. B. Kothe, and C. Zemach, A continuum method for modeling surface tension, J. Comput. Phys. **100**, 335 (1992).

31 Z. Guo, D. F. Fletcher, and B. S. Haynes, Implementation of a height function method to alleviate spurious currents in CFD modelling of annular flow in microchannels, Appl. Math. Model. **39**, 4665 (2015).

32 M. Malik, E. S. C. Fan, and M. Bussmann, Adaptive VOF with curvature-based refinement, Numer. Methods Fluids **55**, 693 (2007).

33 Y. Hu, Q. Wu, H. Zhang, B. Huang, and G. Wang, Verification and validation for large eddy simulation of the turbulent flow around an underwater entity, Phys. Fluids **35**, 125128 (2023).

34 L. E. Borgman, Directional Spectra Models for Design Use: Offshore Technology Conference (Dallas, Texas: 1969721-736).

35 Y. Yu, Numerical simulation and prediction of ocean wave, J. Dalian Univ. Technol. **48**, 84 (1981).

基于动量源项造波的数值波浪水池验证与确认研究

张后胜, 胡宜静, 黄彪, 赵欣

摘要 本文针对一种动量源项造波方法开展了系统的验证和确认(V&V)研究. 首先对规则波和随机波数值水池的一些参数进行了优化. 之后采用H2-5 V&V方法, 包含五套网格, 网格细化率为1.225, 用于验证规则波的数值波浪水池, 主要针对三级(H_s = 0.75 m)和六级(H_s = 5 m)规则波浪的波高和质量守恒对规则波数值水池开展验证研究. 此外, 还选择了八种不同的海况开展规则波浪的波高、质量守恒和波频确认研究. 关于随机波数值波浪水池, 选择了五种不同的海况, 其有效波高在0.09 m至12.5 m之间, 以验证随机波浪的统计特征, 包括波浪谱谱形、峰值频率和有效波高. 结果表明, 在最精细的网格上, 3级和6级规则波的波高验证误差分别为−0.018和−0.35, 质量守恒验证误差分别是−0.14和−0.17. 不确定性分析表明, 通过调整网格尺寸, 数值误差可以被建模误差部分抵消, 从而获得较小的确认误差. 不同海况下规则波的波高、质量守恒和频率的确认误差分别不超过7%、8%和2%. 对于3级(H_s = 0.75 m)和6级(H_s = 5 m)规则波, 分别在安全系数$FS \approx 1$和$FS \approx 0.5$~1的情况下, 对波浪发展段的波高进行了确认. 随机波浪的有效波高和峰值频率的确认误差均小于2%.